

# Doppler follow-up of OGLE transiting companions in the Galactic bulge<sup>★</sup>

F. Bouchy<sup>1,4</sup>, F. Pont<sup>1,4</sup>, C. Melo<sup>2</sup>, N.C. Santos<sup>3,4</sup>, M. Mayor<sup>4</sup>, D. Queloz<sup>4</sup> and S. Udry<sup>4</sup>

<sup>1</sup> Laboratoire d'Astrophysique de Marseille, Traverse du Siphon, BP8, 13376 Marseille Cedex 12, France

<sup>2</sup> European Southern Observatory, Casilla 19001, Santiago 19, Chile

<sup>3</sup> Centro de Astronomia e Astrofísica da Universidade de Lisboa, Tapada da Ajuda, 1349-018 Lisboa, Portugal

<sup>4</sup> Observatoire de Genève, 51 ch. des Maillettes, 1290 Sauverny, Switzerland

Received ; accepted

**Abstract.** Two years ago, the OGLE-III survey (Optical Gravitational Lensing Experiment) announced the detection of 54 short period multi-transiting objects in the Galactic bulge (Udalski et al., 2002a, 2002b). Some of these objects were considered to be potential hot Jupiters. In order to determine the true nature of these objects and to characterize their actual mass, we conducted a radial velocity follow-up of 18 of the smallest transiting candidates. We describe here our procedure and report the characterization of 8 low mass star transiting companions, 2 grazing eclipsing binaries, 2 triple systems, 1 confirmed exoplanet (OGLE-TR-56b), 1 possible exoplanet (OGLE-TR-10b), 1 clear false positive and 3 unsolved cases. The variety of cases encountered in our follow-up covers a large part of the possible scenarii occurring in the search for planetary transits. As a by-product, our program yields precise masses and radii of low mass stars.

**Key words.** techniques: radial velocities – binaries: eclipsing – stars: low-mass, brown dwarfs – planetary systems

## 1. Introduction

Since 1995 the search for planets by radial velocity surveys has lead to the detection of more than 120 planetary candidates. The diversity of orbital characteristics, the mass distribution of the planets (actually only the  $m \sin i$ ) and its link with brown dwarfs and low-mass stars as well as the characteristics of host stars prompted a reexamination of planetary formation theory (e.g., Udry et al. 2003, Santos et al. 2003, Eggenberger et al. 2004). The most unexpected fact was the existence of extrasolar giant planets (EGPs) in very short orbits. Extra mechanisms, not envisioned by the study of our Solar system, have been suggested to explain these objects, like the migration of planets in the proto-planetary disk and gravitational interactions (e.g., Goldreich & Tremaine 1980, Lin et al. 1996).

Monitoring of photometric transits caused by an EGP passing on the disk of its hosting star and obscuring part of its surface provides an opportunity to determine its actual size. When combined with spectroscopic observations, it leads to the unambiguous characterization of the two fundamental parameters (mass and radius) used for internal structure studies of EGPs. The discovery of HD209458 by both Doppler measurements (Mazeh et al. 2000) and photometric transit (Charbonneau et

al. 2000; Henry et al. 2000) led to the first complete characterization of an EGP, illustrating the real complementarity of the two methods. These last years many extensive ground-based photometric programs have been initiated to detect transits by short period EGPs (Horne 2003). The OGLE-III survey (Optical Gravitational Lensing Experiment) announced recently the detection of 137 short-period multi-transiting objects (Udalski et al., 2002a, 2002b, 2002c, 2003). The estimated radius of these objects range from 0.5 Jupiter radius to 0.5 solar radius and their orbital periods range from 0.8 to 8 days. The smallest objects could be suspected to be EGPs, but considering only the radius measured by OGLE, one can not conclude on the planetary nature of the objects per se. They could as well be brown-dwarf or low-mass stars since in the low mass regime the radius is independent of the mass (Guillot, 1999). No information on the mass of these companions is given by the transit measurements. Doppler follow-up of these candidates is the only way to confirm the planetary, brown-dwarf or low-mass star nature of the companions. Planetary transit detection suffers also some ambiguity related to the configuration of the system. The radial velocity measurement is therefore very important in that respect to discriminate true central transits from other cases due to, for example, grazing eclipsing binaries, blended system and stellar activity. The spectroscopy of the central star, which is a by-product of radial velocity measurement, is necessary to constrain the star radius and therefore the companion radius. The measurement of the true mass of a

Send offprint requests to: Francois.Bouchy@oamp.fr

<sup>★</sup> Based on observations collected with the UVES and FLAMES spectrographs at the VLT/UT2 Kueyen telescope (Paranal Observatory, ESO, Chile: program 70.C-0209 and 71.C-0251)

companion by the radial velocity orbit, coupled with the measurement of its radius, lead to a direct measurement of its mean density, an essential parameter for the study of internal structure of EGP, brown dwarfs and low mass stars.

The difficulties of Doppler follow-up of OGLE candidates come from the faintness of the stars (with V magnitudes in the range 14-18). The fields, which are located in the galactic disk, are furthermore very crowded. To characterize a hot Jupiter, one needs radial velocity precision better than  $100 \text{ m s}^{-1}$  and the capability to distinguish whether the system is blended or not by a third star like the triple system HD41004 (Santos et al., 2003).

Several teams are involved in the Doppler follow-up of OGLE candidates. Konacki et al. (2003a) announced first that the companion of OGLE-TR-56 is a planet of 0.9 Jupiter mass. Dreizler et al. (2003) gave an upper limit of 2.5 Jupiter mass for the companion of OGLE-TR-3. This object was however refuted by Konacki et al. (2003b) who also gave informations on 3 other OGLE companions (OGLE-TR-10, 33 and 58). Additional measurements, conducted by Torres et al. (2004a), lead to improve the mass determination of OGLE-TR-56b to 1.45 Jupiter mass. Recently, we announced the characterization of planets OGLE-TR-113b, OGLE-TR-132b (Bouchy et al. 2004, Moutou et al. 2004) and OGLE-TR-111b (Pont et al. 2004).

We present in this paper the Doppler follow-up observations of 18 OGLE multi-transiting companions (OGLE-TR-5, 6, 7, 8, 10, 12, 17, 18, 19, 33, 34, 35, 48, 49, 55, 56, 58 and 59) from the 54 detected in the Galactic bulge (Udalski et al., 2002a, 2002b).

## 2. Target selection and observations

### 2.1. UVES

We have obtained 16 hours in service mode with the UVES spectrograph on the ESO-VLT in October 2002 (program 70C.0209A). For this run we selected 3 candidates (OGLE-TR-8, 10 and 12) with an estimated companion radius less than 1.6 Jupiter radius (following the value given by Udalski et al., 2002a). We were aware that UVES has no fiber to produce a stable illumination at the entrance of the spectrograph and that the Iodine cell method is unusable for such faint stars. However, using the smallest slit (0.3 arcsec) in a medium seeing condition (0.9-1.4 arcsec), we can minimize the velocity error stemming from the shift of the photo-center on the slit. Considering as well the very good guiding ( $< 0.1$  arcsec) and the centering accuracy of UT2 (about 0.1 arcsec), we simulated that for a 1.0 arcsec seeing one should reach an overall stabilization of the photo-center of about  $1/70$  of the slit width. This corresponds to a radial velocity error of about  $40 \text{ m s}^{-1}$ . In order to check our accuracy we added the bright standard radial velocity star HD162907 (selected from the CORALIE exoplanet survey) close to our 3 candidates. Moreover, in order to track and to correct instrumental calibration drifts we took Thorium exposures before and after each science exposures. With such a procedure we expected an overall radial velocity precision of about  $50 \text{ m s}^{-1}$ . We used the red arm of the spec-

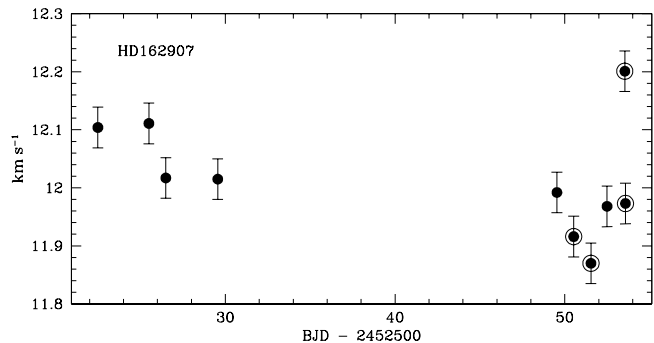


**Fig. 1.** Doppler measurements of the standard star HD162907 made with UVES. The dispersion of  $93 \text{ m s}^{-1}$  is dominated by the centering error. Encircled points correspond to measurements made with a seeing lower than 0.9 arcsec.

trograph with a central wavelength of 580 nm. Notice that in order to reach this precision it is mandatory not to conduct this program in good seeing conditions (i.e seeing less than 0.9 arcsec). We noticed that such an unusual requirement is extremely rare in Paranal. We made 8 measurements of each targets with exposure time between 20 and 40 minutes. Figure 1 shows the result obtained with UVES on HD162907. The dispersion of  $93 \text{ m s}^{-1}$  is dominated by the centering error especially during night with good seeing condition. If we eliminate the 4 measurements made with a seeing lower than 0.9 arcsec, the dispersion reaches  $54 \text{ m s}^{-1}$ .

### 2.2. FLAMES

The FLAMES facilities on the VLT (available since march 2003) seems to be the most efficient way to conduct the Doppler follow-up of OGLE candidates. FLAMES is a multi-fiber link which allows to feed the spectrograph UVES with up to 7 targets on a field-of-view of 25 arcmin diameter in addition with the simultaneous thorium calibration. The fiber link allows for a stable illumination at the entrance of the spectrograph and the simultaneous thorium calibration is used to track instrumental drift. Forty five minutes on a 17 magnitude star reach a signal-to-noise ratio of about 8, corresponding to a photon noise uncertainty of about  $25 \text{ m s}^{-1}$  on a non-rotating K dwarf star. We have obtained 24 hours in service mode on this instrument (program 71.C-0251A) in order to observe in May and June 2003 17 candidates (OGLE-TR-5, 6, 7, 10, 12, 17, 18, 19, 33, 34, 35, 48, 49, 55, 56, 58 and 59) located in 3 FLAMES fields (see Fig. 2). For this program, we selected a sample including 7 candidates with an estimated companion radius less than 1.6 Jupiter radius (following the value given by Udalski et al., 2002a, 2002b) and completed each fields with targets having larger companion radius in order to bring constraint in the mass-radius relation of low-mass stars.

### 2.3. HARPS

HARPS is a new fiber-fed spectrograph on the ESO 3.6-m telescope (Mayor et al. 2003) dedicated to high-precision Doppler measurements. During the second commissioning in

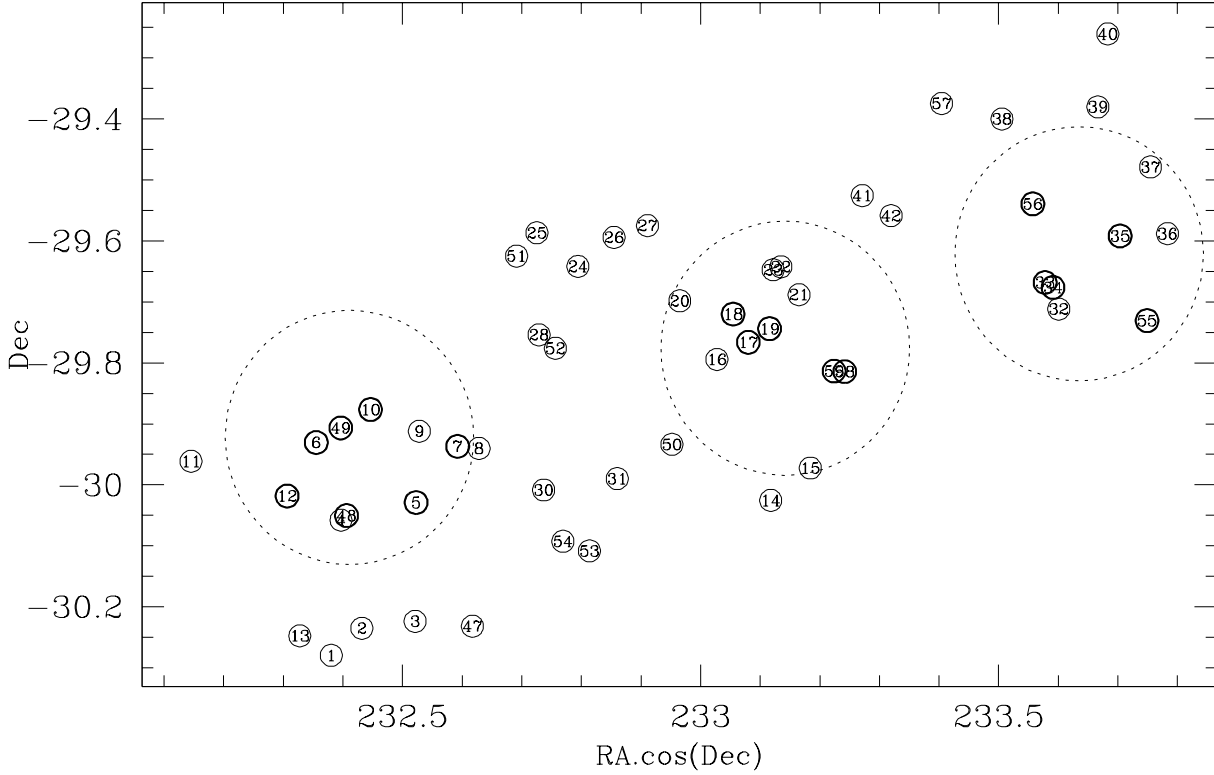


**Fig. 2.** Positions of the 54 OGLE candidates on the sky and localization of our 3 selected FLAMES fields. Bold circles correspond to the 17 observed OGLE candidates during our run.

June 2003, we tested the capability of the instrument to realize radial velocity measurements on faint stars and made 5 measurements of 1-hour exposure on OGLE-TR-56. The 20 first blue spectral orders were not used to compute radial velocity due to their too low S/N ( $< 1$ ).

### 3. Spectroscopic analysis

#### 3.1. Radial velocities

The spectra obtained from the FLAMES and UVES spectrographs were extracted using the standard ESO-pipeline with bias, flat-field and background correction. Wavelength calibration was performed with ThAr spectra. The radial velocities were obtained by weighted cross-correlation with a numerical mask constructed from the Sun spectrum atlas. In the case of FLAMES and HARPS, the simultaneous ThAr spectrum was used in order to compute the instrumental drift by cross-correlation with a Thorium mask. Radial velocity uncertainties (in  $\text{km s}^{-1}$ ) were computed as a function of the SNR per pixel of the spectrum, the width (FWHM in  $\text{km s}^{-1}$ ) and depth (C in %) of the Cross-Correlation Function (CCF) through the following relation based on photon noise simulations:

$$\sigma_{\text{RV}} = \frac{3 \cdot \sqrt{\text{FWHM}}}{\text{SNR} \cdot C}.$$

However, our measurements are clearly not photon noise limited and we added quadratically an empirically determined uncertainty of  $35 \text{ m s}^{-1}$  in order to take into the account systematic errors probably due to wavelength calibration errors,

fiber-to-fiber contamination, and residual cosmic rays. We checked that, on non-rotating dwarf stars, the O-C residuals of our measurements are in agreement with the estimated uncertainties based on this relation. Our best O-C residuals indicate that we reached radial velocity precision lower than  $100 \text{ m s}^{-1}$ .

Our radial velocity measurements and Cross-Correlation Function parameters are listed in Table 1. For some candidates observed with FLAMES at very low SNR ( $\text{SNR} < 5$ ), the depth of the CCF is correlated with the SNR. This is a clear indication that the spectra are contaminated by background light due in part to the fiber-to-fiber contamination. We take into consideration this effect in order to correctly estimate the SNR and to compute our radial velocity uncertainties more strictly. Phase-folded radial velocities and results are presented and discussed in section 5.

#### 3.2. Rotation velocities

For each object, the eight observed cross-correlation functions were shifted by the observed radial velocity and co-added to give a combined CCF of higher signal-to-noise ratio. Rotationally broadened line profiles were convolved with a Gaussian instrumental profile depending of the instrument and correlation mask:  $\sigma = 3.0 \text{ km s}^{-1}$  for UVES and  $4.0 \text{ km s}^{-1}$  for FLAMES. The instrumental profile was determined with HD162907 for UVES and the combined spectrum of OGLE-TR-19 and OGLE-TR-49 for FLAMES. We also checked the

**Table 1.** Radial velocity measurements (in the barycentric frame) and CCF parameters. Label *a* and *b* indicate that 2 components are present in the CCF. BJD in the range [522-557], [750-798] and [809-812] correspond respectively to UVES, FLAMES and HARPS measurements.

BJD [−2452000 d]	RV [km s <sup>−1</sup> ]	depth [%]	FWHM [km s <sup>−1</sup> ]	SNR	$\sigma_{RV}$ [km s <sup>−1</sup> ]
OGLE-5					
759.72111	−15.452	1.88	119.4	8.9	1.959
764.85708	13.273	2.17	151.5	7.6	2.239
766.79458	48.733	2.28	116.7	11.6	1.226
767.72839	12.256	1.83	142.5	8.8	2.224
768.84710	−11.662	2.56	119.0	15.5	0.825
769.85598	55.993	2.33	121.4	10.0	1.419
770.82050	60.894	2.34	122.9	11.0	1.293
797.76880	−34.035	2.40	123.3	11.3	1.229
OGLE-6					
759.72111	33.160	7.34	35.4	5.0	0.488
764.85708	46.860	9.95	34.9	6.4	0.281
766.79458	−10.166	10.93	34.0	7.1	0.228
767.72839	−10.385	8.99	33.2	5.6	0.345
768.84710	33.995	13.55	38.0	10.5	0.135
769.85598	44.341	10.22	36.2	6.1	0.292
770.82050	8.344	12.33	35.0	7.2	0.203
797.76880	24.197	11.86	36.6	7.5	0.207
OGLE-7					
759.72111	8.454	6.94	55.3	9.6	0.337
764.85708	20.473	7.13	54.6	10.4	0.301
766.79458	−11.924	8.32	54.8	11.3	0.239
767.72839	14.997	6.79	48.6	9.5	0.326
768.84710	−42.394	8.04	54.7	14.4	0.195
769.85598	10.541	7.13	50.4	10.9	0.276
770.82050	−6.034	7.48	50.6	11.2	0.257
797.76880	9.175	7.30	52.4	12.0	0.250
OGLE-8a					
522.55485	19.193	10.94	16.9	6.9	0.167
526.55409	69.882	11.60	18.1	8.6	0.133
549.59728	29.917	10.50	16.8	4.1	0.288
550.58081	−54.831	11.04	17.3	5.1	0.224
551.59645	−78.950	11.02	17.7	5.9	0.197
552.54163	−17.312	11.72	17.9	7.2	0.154
553.59422	64.676	10.67	17.4	5.9	0.202
556.50991	−79.423	10.34	17.0	4.2	0.287

BJD [−2452000 d]	RV [km s <sup>−1</sup> ]	depth [%]	FWHM [km s <sup>−1</sup> ]	SNR	$\sigma_{RV}$ [km s <sup>−1</sup> ]
OGLE-8b					
522.55485	−27.289	10.33	16.1	6.9	0.172
526.55409	−80.238	10.35	16.7	8.6	0.142
549.59728	−37.875	9.54	17.3	4.1	0.321
550.58081	48.938	9.70	17.1	5.1	0.253
551.59645	74.409	10.02	17.7	5.9	0.216
552.54163	10.650	9.87	17.2	7.2	0.179
553.59422	−74.939	10.29	15.4	5.9	0.197
556.50991	74.659	9.14	15.4	4.2	0.309
OGLE-10					
522.50823	−6.421	30.62	11.7	6.1	0.065
525.50905	−6.413	30.14	11.9	6.8	0.061
526.51146	−6.485	29.06	10.7	6.9	0.060
549.55329	−6.607	29.94	11.9	4.4	0.086
550.53700	−6.135	29.86	11.5	3.4	0.106
551.55409	−6.475	30.28	11.2	3.8	0.094
552.50287	−6.410	31.03	11.9	6.4	0.063
553.54729	−6.135	30.58	11.3	6.4	0.062
759.72111	−6.291	24.03	12.9	8.4	0.064
764.85708	−6.236	27.18	13.1	10.9	0.051
766.79458	−6.212	26.17	13.1	9.8	0.055
767.72839	−6.274	25.11	12.5	9.0	0.059
768.84710	−6.365	27.19	12.8	14.6	0.044
769.85598	−6.238	25.91	12.9	9.9	0.055
770.82050	−6.105	26.89	12.5	15.3	0.043
797.76880	−6.130	26.80	12.6	11.2	0.050
OGLE-12					
522.52429	−10.897	27.06	11.8	8.0	0.059
525.52490	43.661	27.50	11.7	8.1	0.058
526.52813	57.877	27.47	12.0	9.0	0.055
549.57081	−0.796	26.78	12.3	5.4	0.081
550.55534	21.265	27.57	11.5	4.3	0.093
551.57020	45.212	27.21	11.6	7.0	0.064
552.51801	58.079	27.61	12.2	7.4	0.062
553.56592	54.157	26.78	12.3	5.6	0.078
759.72111	52.149	20.08	12.9	6.6	0.089
764.85708	−10.531	22.86	12.4	8.0	0.068
766.79458	16.577	23.38	13.3	9.3	0.061
767.72839	39.484	21.31	12.8	8.2	0.071
768.84710	57.534	24.75	13.2	15.4	0.045
769.85598	56.098	22.96	12.6	8.0	0.068
770.82050	39.236	24.05	13.2	11.6	0.052
797.76880	15.003	23.58	12.8	9.4	0.060

instrumental profile on both spectrographs with the ThAr spectrum. The profiles were fitted to the CCF to determine the projected rotation velocity  $v \sin i$  of the target objects. The result is displayed in Table 2. A quadratic limb-darkening with coefficients  $u_1 + u_2 = 0.6$  was assumed. The computations of Barban et al. (2003) find that such a coefficient is a suitable approximation for a wide range of spectral types in wavelengths corresponding to the V filter.

For close binaries, with rotation periods of the order of a few days, we expect that the rotation axis is aligned with the orbital axis, the orbit is circularized and the system is tidally locked (e.g., Levato 1976, Hut 1981, Melo et al. 2001). For known close binaries, the alignment of the axes and the tidal locking are observed to be effective even before orbital circularization. It can therefore be expected that in cases of a massive

transiting companion with a short period, the system is tidally locked and  $v \sin i$  is large. In that case,  $P_{rot} = P_{transit}$  and the rotational velocity is directly related to the radius of the primary. Rotation velocities observed in our sample are generally compatible with the hypothesis of tidal locking. In these cases  $v \sin i$  provides a measurement of  $R$  with an estimated accuracy of a few percent. The uncertainty in the determination of  $v \sin i$  was estimated by computing values on each of the individual CCF and calculating the dispersion of these values. In most cases this "formal" uncertainty is very small, and the dominant source of error is actually the adopted value of the limb darkening coefficient (see Section 6). For the smallest rotational velocities ( $v \sin i < 5 \text{ km s}^{-1}$ ), the dominant uncertainty becomes the adopted value of the instrumental broadening and the stellar

BJD [−2452000 d]	RV [ $\text{km s}^{-1}$ ]	depth [%]	FWHM [ $\text{km s}^{-1}$ ]	SNR	$\sigma_{\text{RV}}$ [ $\text{km s}^{-1}$ ]
OGLE-17					
759.75994	−64.941	26.73	10.0	7.7	0.058
764.81842	−9.416	26.36	10.3	6.1	0.069
766.84092	−2.377	26.49	9.8	6.9	0.062
767.76871	−8.671	17.55	9.3	3.8	0.142
768.76694	−19.328	28.28	10.0	8.5	0.053
769.81610	−32.710	26.32	10.1	7.5	0.060
770.90035	−46.353	24.91	9.7	6.5	0.067
791.72546	−21.462	26.47	9.9	7.5	0.059
OGLE-18					
759.75994	−24.248	4.67	87.5	8.4	0.716
764.81842	−12.247	4.13	72.2	7.1	0.870
766.84092	0.683	4.26	66.8	7.3	0.789
767.76871	−91.001	3.75	60.9	5.0	1.249
768.76694	−8.342	4.55	78.8	8.9	0.659
769.81610	−73.094	4.90	69.6	8.2	0.624
770.90035	−23.657	4.29	82.5	7.1	0.895
791.72546	−29.868	4.23	81.9	8.4	0.765
OGLE-19					
759.75994	−33.380	25.46	10.0	5.3	0.078
764.81842	−33.245	24.85	9.5	4.9	0.084
766.84092	−33.287	25.14	9.9	4.8	0.086
767.76871	−33.385	17.80	9.3	3.6	0.148
768.76694	−33.087	29.12	9.9	5.9	0.065
769.81610	−33.244	25.75	9.8	5.2	0.078
770.90035	−33.394	23.78	10.2	4.6	0.095
791.72546	−33.414	24.53	9.6	5.2	0.080
OGLE-33a					
764.89532	−28.500	4.00	61.2	17.2	0.343
766.87982	−28.500	4.00	61.2	16.0	0.368
767.80618	−28.500	4.00	61.2	15.6	0.378
769.77114	−28.500	4.00	61.2	16.9	0.349
770.85930	−28.500	4.00	61.2	16.1	0.366
790.70926	−28.500	4.00	61.2	16.8	0.351
797.73001	−28.500	4.00	61.2	17.1	0.345
OGLE-33b					
764.89532	1.895	0.70	52.0	17.2	1.797
766.87982	9.212	0.60	51.0	16.0	2.232
767.80618	−63.941	1.00	48.0	15.6	1.333
769.77114	−62.742	1.00	53.0	16.9	1.293
770.85930	26.163	0.40	49.0	16.1	3.261
790.70926	22.695	0.50	52.0	16.8	2.576
797.73001	−60.852	1.10	49.0	17.1	1.117

micro-turbulence parameter. In order to take into account such systematic uncertainties we fix afterward the lowest uncertainty of  $v \sin i$  to  $1 \text{ km s}^{-1}$ .

### 3.3. Stellar spectroscopic parameters

For the slowly-rotating stars in our sample, the stellar parameters (temperatures, gravities and metallicities) were obtained from an analysis of a set of Fe I and Fe II lines, following the procedure used in Santos et al. (2004). Line equivalent widths were derived using IRAF<sup>1</sup>, and the abundances were obtained

<sup>1</sup> distributed by NOAO, AURA, Inc., under contract with the NSF, USA.

BJD [−2452000 d]	RV [ $\text{km s}^{-1}$ ]	depth [%]	FWHM [ $\text{km s}^{-1}$ ]	SNR	$\sigma_{\text{RV}}$ [ $\text{km s}^{-1}$ ]
OGLE-34					
759.79751	32.726	21.74	12.3	6.5	0.082
764.89532	88.686	20.53	11.3	6.8	0.080
766.87982	46.630	18.25	11.6	4.9	0.119
767.80618	33.753	16.82	11.2	4.6	0.134
769.77114	53.710	20.40	12.3	5.6	0.099
770.85930	78.537	19.60	11.3	5.3	0.103
790.70926	88.310	20.55	10.9	5.5	0.094
797.73001	96.514	19.70	12.1	5.7	0.099
OGLE-35a					
759.79751	−145.398	3.74	58.6	16.8	0.367
764.89532	−134.986	3.63	57.1	17.2	0.365
766.87982	−151.252	3.59	58.0	16.0	0.399
769.77114	−159.365	3.84	59.2	16.9	0.357
770.85930	42.947	3.75	56.7	16.1	0.376
790.70926	10.277	3.47	55.0	16.8	0.383
797.73001	−117.998	3.48	54.9	17.1	0.375
OGLE-35b					
759.79751	21.308	3.78	56.7	16.8	0.357
764.89532	11.174	3.60	55.9	17.2	0.364
766.87982	27.804	3.64	56.8	16.0	0.390
769.77114	35.511	3.78	55.9	16.9	0.353
770.85930	−165.670	3.86	56.6	16.1	0.365
790.70926	−133.420	3.48	55.4	16.8	0.384
797.73001	−3.016	3.42	54.9	17.1	0.382
OGLE-48					
766.79458	−0.392	0.79	203.7	12.5	4.336
767.72839	−0.798	0.89	323.6	7.8	7.774
768.84710	4.351	1.00	232.4	15.8	2.895
770.82050	6.071	1.17	383.9	8.9	5.645
OGLE-49					
759.72111	−106.352	12.44	9.7	2.2	0.338
764.85708	−106.928	13.39	7.4	2.5	0.246
766.79458	−107.230	19.76	9.5	2.7	0.174
767.72839	−106.680	10.80	9.3	2.0	0.434
768.84710	−106.965	25.41	9.1	4.6	0.085
769.85598	−107.327	17.46	9.4	2.6	0.204
770.82050	−106.830	16.52	9.7	2.6	0.218
797.76880	−106.970	20.26	9.4	3.1	0.150

using a revised version of the code MOOG (Sneden 1973), and a grid of Kurucz (1993) atmospheres.

The final parameters have errors of the order of 200 K in  $T_{\text{eff}}$ , 0.40 in  $\log g$ , and 0.20 dex in  $[\text{Fe}/\text{H}]$  (see Table 2). The precision of the derived atmospheric parameters is mostly affected by relatively low S/N of the combined spectra (30-50), together with some possible contamination coming from the ThAr spectrum. Furthermore, blends with the spectrum of a low mass stellar companion or a background star may also affect the determination of the stellar parameters.

For the fast rotating stars in our sample ( $v \sin i \geq 20 \text{ km s}^{-1}$ ), the method described in Santos et al. (2004) is not applicable, given that the measurement of individual equivalent widths is not accurate enough due to line-blending. In these cases we have adopted a simpler approach, and have determined very approximate effective temperatures for the stars by visual comparison of the combined spectra with synthetic

BJD [−2452000 d]	RV [km s <sup>−1</sup> ]	depth [%]	FWHM [km s <sup>−1</sup> ]	SNR	$\sigma_{RV}$ [km s <sup>−1</sup> ]
OGLE-55					
759.79751	−12.937	5.62	49.2	7.0	0.536
764.89532	5.990	5.55	50.7	7.3	0.528
766.87982	24.803	4.20	48.4	5.8	0.857
767.80618	20.569	5.18	53.1	5.2	0.812
769.77114	9.084	5.73	53.1	6.0	0.637
770.85930	26.478	5.38	46.4	6.4	0.595
790.70926	−12.510	4.66	43.5	5.4	0.787
797.73001	−21.156	5.47	49.1	7.5	0.514
OGLE-56					
759.79751	−48.284	30.47	10.1	12.2	0.043
764.89532	−48.528	30.83	10.2	11.6	0.044
766.87982	−48.241	29.47	10.7	9.2	0.050
767.80618	−48.279	27.69	10.5	8.0	0.056
769.77114	−48.516	29.69	10.3	10.3	0.047
770.85930	−48.485	29.44	10.5	9.8	0.049
790.70926	−48.306	28.20	10.3	9.0	0.052
797.73001	−48.518	29.11	10.1	9.9	0.048
809.76233	−48.550	36.90	8.1	2.7	0.087
810.59822	−48.126	40.30	8.6	2.3	0.094
810.83456	−48.440	37.40	9.1	2.3	0.107
811.63656	−48.011	40.10	8.2	3.8	0.057
811.83617	−48.212	39.50	8.1	3.0	0.073
OGLE-58					
759.75994	51.016	11.48	13.1	15.6	0.070
764.81842	51.091	11.69	12.6	13.8	0.075
766.84092	51.115	11.54	13.0	14.4	0.074
767.76871	51.200	11.04	12.6	10.5	0.098
768.76694	51.169	11.70	12.7	16.5	0.066
769.81610	51.051	11.60	13.0	15.1	0.071
770.90035	50.996	11.35	13.1	13.8	0.078
791.72546	51.004	11.38	12.9	15.3	0.071
OGLE-59a					
759.75994	9.765	3.32	49.4	13.3	0.479
764.81842	8.670	3.30	49.5	10.8	0.593
766.84092	9.714	3.30	46.6	12.0	0.518
767.76871	8.835	3.30	49.5	8.0	0.800
768.76694	8.890	3.43	51.3	14.1	0.446
769.81610	8.119	3.43	49.6	12.9	0.479
770.90035	9.113	3.30	49.5	10.8	0.593
791.72546	9.363	3.30	49.5	12.4	0.517
OGLE-59b					
759.75994	61.728	2.28	27.0	13.3	0.515
764.81842	3.619	3.11	36.7	10.8	0.542
766.84092	−44.414	2.82	28.6	12.0	0.475
767.76871	−2.520	2.46	27.2	8.0	0.796
768.76694	60.252	2.63	25.3	14.1	0.408
769.81610	−44.422	2.89	26.4	12.9	0.415
770.90035	13.946	2.92	34.8	10.8	0.562
791.72546	−1.157	3.70	35.5	12.4	0.391

spectra convolved with a rotational profile to take into account the projected rotational velocity.

Stellar spectroscopic parameters are given in Table 2. The lines of OGLE-TR-48 are too rotationally broadened for a spectral type estimation. Our  $\log g$  and  $[Fe/H]$  estimates are all very uncertain, they simply indicate that the target objects are dwarfs and have solar or above-solar metallicities.

**Table 2.** Parameters from the spectroscopic analysis. Rotation velocities  $v \sin i$  are computed from the analysis of the CCF.  $T_{eff}$ ,  $\log g$ ,  $[Fe/H]$ : temperature, gravity and metallicity are computed from the analysis of the spectral lines in case of low  $v \sin i$ . For high rotation,  $T_{eff}$  was estimated roughly by comparison with synthetic spectrum. Spectral type of binaries (identified with label *a* and *b*) which include two moving components in the spectra was not possible to determine.

Name	$v \sin i$ [km s <sup>−1</sup> ]	$T_{eff}$ [K]	$\log g$	$[Fe/H]$
5	$87.8 \pm 1.8$	$6700 \pm 500$	-	-
6	$22.6 \pm 0.3$	$5700 \pm 500$	-	-
7	$30.7 \pm 0.2$	$6500 \pm 500$	-	-
8a	$11.7 \pm 0.3$	-	-	-
8b	$11.3 \pm 0.4$	-	-	-
10	$7.7 \pm 0.1$	$6220 \pm 140$	$4.70 \pm 0.34$	$0.39 \pm 0.14$
12	$7.7 \pm 0.2$	$6440 \pm 300$	$4.90 \pm 0.35$	$0.30 \pm 0.26$
17	<5	$5870 \pm 190$	$4.80 \pm 0.45$	$-0.06 \pm 0.21$
18	$44.3 \pm 0.9$	$6500 \pm 500$	-	-
19	$6.0 \pm 0.2$	$5250 \pm 300$	$4.0 \pm 0.50$	$-0.10 \pm 0.30$
33a	$45.3 \pm 0.5$	$6700 \pm 500$	-	-
33b	$\sim 32$	-	-	-
34	$6.3 \pm 0.3$	$6520 \pm 340$	$4.50 \pm 0.48$	$0.32 \pm 0.31$
35a	$34.3 \pm 1.1$	-	-	-
35b	$34.8 \pm 0.8$	-	-	-
48	>100	-	-	-
49	<5	$5000 \pm 500$	-	-
55	$30.5 \pm 0.6$	$6000 \pm 500$	-	-
56	<5	$5970 \pm 150$	$4.20 \pm 0.38$	$0.17 \pm 0.19$
58	$14.6 \pm 0.1$	$6500 \pm 500$	-	-
59a	$34.1 \pm 0.7$	-	-	-
59b	$20.9 \pm 1.1$	-	-	-

A spectral classification of 7 of our targets (OGLE-TR-5, 6, 8, 10, 12, 19 and 35) was previously done by Dreizler et al. (2002). Our stellar spectroscopic parameters determination is in agreement with their result.

## 4. Light curve analysis

### 4.1. Existence and periodicity of transit signal

When the amplitude of the radial velocity variation is small, which may indicate the presence of a planet or a blend with a background eclipsing binary, one must first consider the possibility that the detected photometric signal is not a bona fide transit/eclipse, or that the period of the signal is incorrect. The OGLE photometric data is subject to systematic intra-night drifts in calibration to the level of the hundredth of magnitude, similar to the depth of the smallest detected transit signal. Given the fact that the transit candidates were detected among about 60'000 light curves, it is not impossible that some of them are artefacts. Either the whole detection is spurious or, more likely, one of the detected transit is an artifacts. If there are only two detected transits, this would imply that the periodicity of the event is unknown, and therefore that no information can be derived from the absence of radial velocity variations.

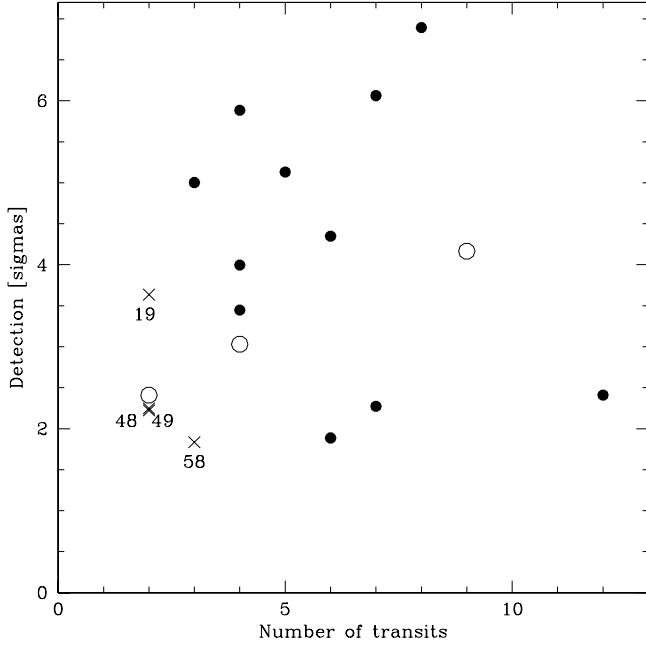


**Fig. 3.** Number of detected transits vs.  $d/\sigma$ , where  $d$  is the depth of the transit signal and  $\sigma$  the photometric uncertainty. Open symbols indicate objects for which the period had to be modified according to the radial velocity data (OGLE-TR-12, 17 and 59), crosses the objects for which no radial velocity variation was detected.

To quantify the reliability of the transit detection, we divided the value of the transit depth by its uncertainty, yielding a “confidence factor” for the existence of the transit, and plotted this factor as a function of the number of transits (see Fig. 3). Objects with only two or three detected transits and a low confidence factor are more likely to be artefacts. This is the case of objects OGLE-TR-19, 48, 49 and 58 which are possible spurious transit detections and are discussed individually below (Section 5.4 and Fig. 10).

In cases when the radial velocity data does not obviously confirm the period of the transit candidates, we also studied the light curve to see if the transit signal were compatible with other periods. For instance, in a two-transit case, several divisors of the interval between the two transits can be possible to put the data in phase. For OGLE-TR-12, 17 and 59, another period than the one given by Udalski et al. (2002a, 2002b) was found to phase the light curve and radial velocity data perfectly. In case of equal mass double-line eclipsing binaries (OGLE-TR-8 and 35), the right period is twice the OGLE period due to the fact that both transits and anti-transits are present in the photometric curve.

#### 4.2. Sinusoidal variations in the light curve

As repeated in Sirko & Paczynski (2003), close binaries can induce variability to the mmag level in the light curve in phase with the transit signal period. If the light of the secondary is not negligible compared to the primary, an anti-transit signal can be visible. Even in the absence of anti-transit, the ellipsoidal

deformation of the primary under the gravitational influence of the secondary causes sinusoidal variations in the light curve with double the phase of the orbital period. Such sinusoidal signals were fitted to the OGLE transit candidate light curve by Sirko & Paczynski (2003).

We have repeated their procedure and find very close results except for the objects for which the period had to be modified according to the radial velocity data (OGLE-TR-12, 17, and 59) and for the SB2 (OGLE-TR-8 and 35). Such procedure clearly indicates that the OGLE-TR-5, 8, 18 and 35 have a massive companion in the stellar mass range.

The periodic sinusoidal signals in the light curves were subtracted when significant from the data before the analysis of the transit shape.

#### 4.3. Analysis of the transit shape

The depth, width and general shape of the transit signal depend on a combination of physical variables, mainly the radius ratio  $\bar{r}$ , the primary radius  $R$  and the impact parameter  $b$  (or, equivalently for circular orbits, the angle  $i$  of the normal of the orbital plane with the line-of-sight) and the orbital eccentricity. It is also more weakly dependent on the total mass ( $m + M$ ) – via the orbital period and semi-major axis for a Keplerian orbit – and the limb darkening coefficients. The parameter  $\bar{r}$  is mainly constrained by the transit depth,  $R \cdot (m + M)^{-1/3}$  by its duration, and  $b$  by its shape. We assumed that all orbits were circular ( $e = 0$ ). Low-period binaries below  $P \sim 10$  days are observed to have circularized orbits (Levato 1976), and all objects in our sample have lower periods except OGLE-TR-17, which indeed shows indications of a small eccentricity in the radial velocity curve (See Section 5.1). In all other cases of large-amplitude variations the radial velocity residuals show no significant variations from a circular orbit.

The light curve were fitted by non-linear least square fitting with analytic transit curves computed according to Mandel & Agol (2002), using a quadratic limb darkening model with  $u_1 + u_2 = 0.3$ . Notice that this is different from the coefficients used for the determination of the rotational velocity, because the wavelengths are different. The OGLE data was obtained with an  $I$  filter while the spectra are centered on the visible. The fitted parameters were  $\bar{r}$ ,  $V_T/R$  and  $b$ , where  $V_T$  is the transversal orbital velocity at the time of the transit.

Broadly, there are two kinds of cases for the transit shape. Either the transit signal is broad and flat and  $b$  has a firm higher bound – a central transit – and in that case  $\bar{r}$  and  $V_T/R$  are very well constrained by the depth and duration of the transit. Or the V-shaped or indefinite signal shape allows for high values of  $b$  – a grazing transit – and in that case  $\bar{r}$  and  $V_T/R$  are correlated with  $b$  and cannot be well determined independently. In real terms, it means that the signal comes either from a small body transiting rapidly across the primary, or a larger body partially obscuring the primary in a slower grazing eclipse. For illustration, Fig. 4 shows the fit of the transits of all our candidates.

The OGLE photometric data is subject to strongly covariant noise. For many objects the systematic drift during the nights – especially near the beginning and end of the night – are of

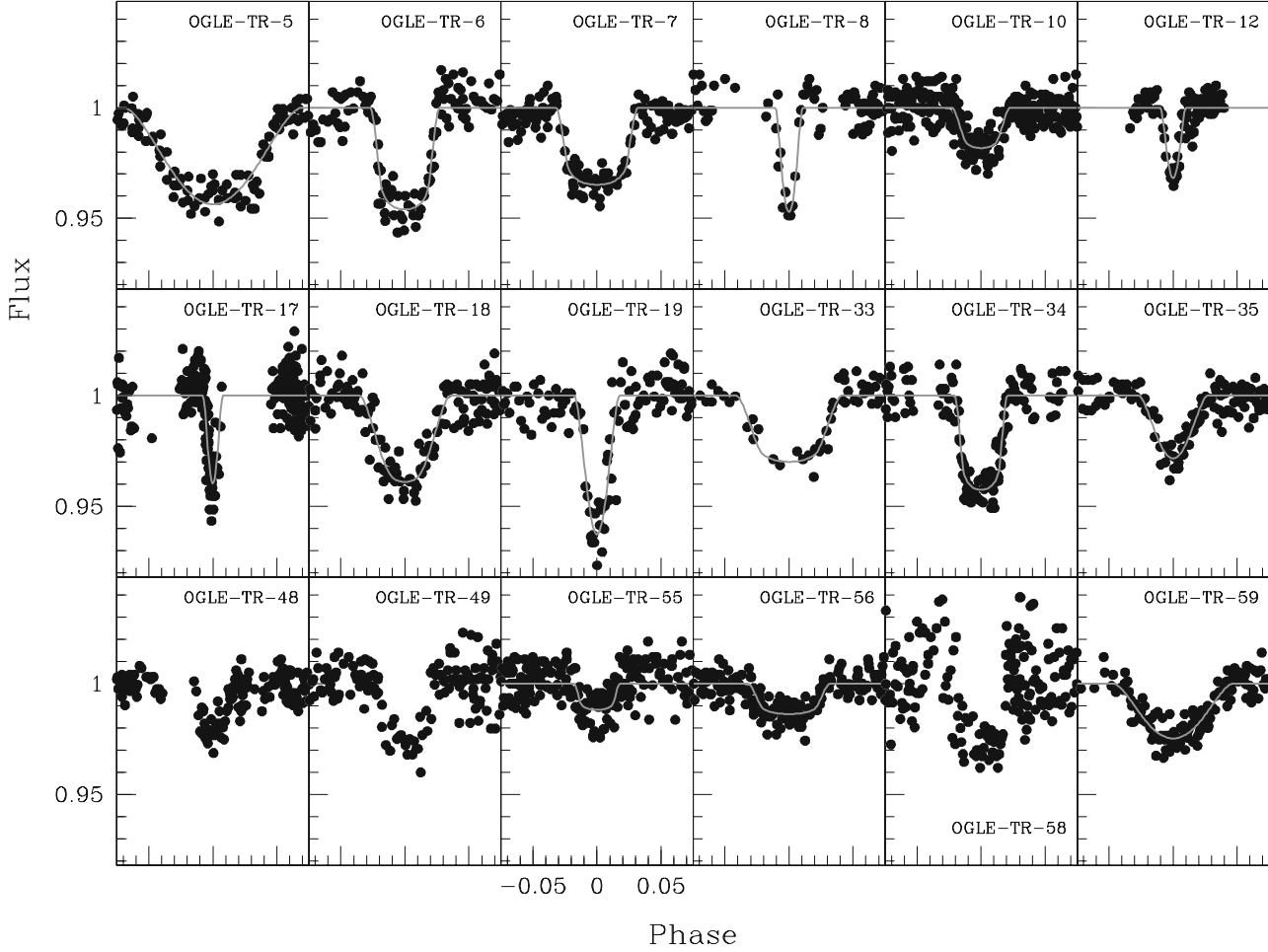


**Fig. 4.** Phase-folded light curve and best-fit transit curve for all the followed OGLE candidates.

the same order as the random noise or even larger (see lowest panel on Fig. 10). Therefore, all the data points cannot be considered as independent estimators on the fitted curve and an error analysis from a chi-square distribution will significantly underestimate the uncertainties.

To compute realistic uncertainties on the values of the transit parameters, we used a technique based on the permutation of the residuals. We compute the residuals by removing the best-fit solution for the transit shape, then exchange the residuals of one night with another randomly chosen night. The fitting procedure is then repeated on the resulting curve with the shuffled residuals, leaving the period as a free parameter. Many Monte Carlo realizations are then carried out to estimate the dispersion of the fitted parameters.

This permutation procedure has the advantage of “letting the data speak by itself” and automatically incorporates the real characteristics of both the random noise and the systematic intra-night drifts. Its use is especially relevant in objects where the transit was covered in a low number of nights. In that case, intra-night systematic drifts can significantly alter the transit shape, and a  $\chi^2$  analysis will yield much too low uncertainties. Figure 5 gives an example of the residual permutation procedure on OGLE-TR-12.

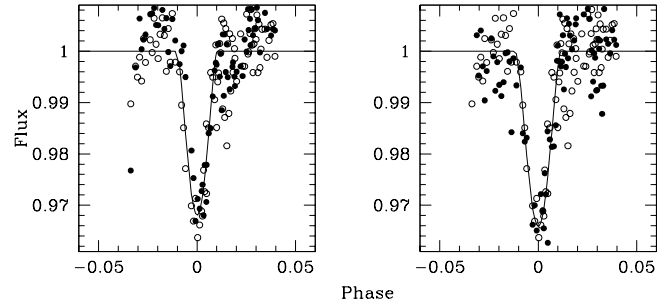


**Fig. 5.** Illustration (for OGLE-TR-12) of the residual permutation method for the estimation of the uncertainties. On both panels, the open symbols indicate the original data, and the dots indicate two realizations (among a total of 100 realizations) of the data with residuals permuted between different nights. The lines indicate the best-fit curve on the permitted data. The resulting  $\bar{\tau}$  is 0.254 and 0.292 respectively. Because the transit coverage is constituted of only two nights, systematic trends in the residuals have a large effect on the resulting parameters. In the case of OGLE-TR-12, this error estimate leads to much higher 1-sigma interval than a  $\chi^2$  analysis.



**Table 3.** Parameters from the transit light curve fit:  $\bar{r}$  radius ratio of the primary and secondary bodies,  $V_T/R$  transit velocity in units of the primary radius,  $b$  impact parameter,  $P$  revisited period according to the radial velocity measurements. We deliberately do not provide the results for the 4 unsolved cases suspected to be false positives OGLE-TR-19, 48, 49 and 58. For the two cases of SB2, stellar parameters were deduced from the spectroscopic orbits and the rotational velocities.

Name	$\bar{r}$	$V_T/R$ [days <sup>-1</sup> ]	$b$	$[b_{down} - b_{up}]$	$P$ [days]
5	$0.189 \pm 0.008$	$22.70 \pm 1.9$	0.56	[0.47-0.65]	0.80827
6	$0.198 \pm 0.006$	$9.76 \pm 0.44$	0.20	[0.00-0.21]	4.54881
7	$0.172 \pm 0.006$	$13.58 \pm 0.50$	0.02	[0.00-0.09]	2.71782
8	-	-	1.65	[1.62-1.68]	5.43284
10	$0.129 \pm 0.007$	$16.80 \pm 1.22$	0.45	[0.00-0.46]	3.10140
12	0.299 [0.26-0.74]	$8.44 \pm 0.83$	1.02	[0.89-1.32]	8.65725
17	0.245 [0.22-0.63]	$8.27 \pm 0.56$	0.90	[0.72-1.28]	13.87370
18	$0.200 \pm 0.020$	$11.78 \pm 0.83$	0.77	[0.73-0.87]	2.22803
19	-	-	-	-	-
33	$0.160 \pm 0.015$	$12.20 \pm 1.25$	0.68	[0.59-0.77]	1.95326
34	$0.188 \pm 0.002$	$6.83 \pm 0.40$	0.00	[0.00-0.02]	8.57633
35	-	-	1.68	[1.65-1.73]	2.51957
48	-	-	-	-	-
49	-	-	-	-	-
55	0.109 [0.107-0.150]	16.45 [9.21-18.72]	0.60	[0.00-0.85]	3.18454
56	$0.114 \pm 0.004$	22.84 [22.43-27.27]	0.69	[0.50-0.69]	1.21192
58	-	-	-	-	-
59	$0.257 \pm 0.089$	$10.238 \pm 0.632$	0.99	[0.82-1.31]	2.99432

#### 4.4. Synthesis of the spectroscopic and photometric constraints

The different constraints are combined by chi-square minimization to obtain an estimate of the physical characteristics of the two bodies involved in the transit. In most cases, constraints overlap and allow one or several coherence checks between the different lines of inquiry.

The measured rotation velocity  $v \sin i$  (in  $\text{km s}^{-1}$ ) is related to the primary radius (in solar unit) and the period (in days) through:

$$v \sin i = 50.6 \cdot \frac{R}{P} \cdot \sin i. \quad (1)$$

For a circular orbit, the semi-amplitude of the radial velocity variation (in  $\text{km s}^{-1}$ ) is related to the masses (in solar unit) and period (in days) through:

$$K = 214 \cdot \frac{m}{(m+M)^{2/3}} \cdot P^{-1/3}. \quad (2)$$

The impact parameter  $b$  and transit velocity per primary radius  $V_T/R$  are related to the orbital and physical parameters  $R$ ,  $m$ ,  $M$  (in solar unit),  $P$  (in days) and  $i$ , for a circular Keplerian orbit, in the following way:

$$b = \frac{a \cdot \cos i}{R}, \quad (3)$$

$$V_T/R = 2\pi \cdot \frac{a}{P \cdot R}, \quad (4)$$

with  $a$  (in solar radius) given by the third Kepler's law:

$$a = 4.20 \cdot P^{2/3} \cdot (m+M)^{1/3}.$$

The radius ratio is obviously related to the stellar radius  $R$  and companion radius  $r$ :

$$\bar{r} = r \cdot R^{-1}. \quad (5)$$

Finally, the spectroscopic determinations of the temperature, gravity and metallicity of the primary provides independent constraints on  $R$  and  $M$  via the stellar evolution models. We used the relation between physical and observable parameters provided by the models of Girardi et al. (2002).

$$(\log T_{eff}, \log g, [Fe/H], R) = f(M, age, Z). \quad (6)$$

The constraints of Equations 1 to 6 were combined by chi-square minimization. In most cases,  $R$  is precisely determined from the rotation velocity. Then  $M$  is constrained on the one hand by the spectroscopic parameters applied by the models, on the other hand by the  $V_T/R$  factor in the fit and the transit curve. Parameter  $r$  then proceeds from  $R$  and  $\bar{r}$ , and  $m$  from  $M$  and  $K$ . Parameter  $i$  is mainly derived from  $b$ . A low value of the minimum  $\chi^2$  ensures that the different constraints are coherent. This procedure yields very satisfactory accuracies on all the derived parameters. Note that the resulting  $r$  and  $m$  are only weakly dependent on the accuracy of the stellar evolution models, because  $R$  is primarily determined from the rotation velocity and  $M$  enters the determination of  $m$  with a 2/3 exponent.

There are two cases for which the accuracy on the final parameters is lower: 1) In cases when high values of  $b$  ( $b \sim 1$ ) are compatible with the light curve data, there is some degeneracy between the impact parameter, the duration of the eclipse and the radius ratio. In that case the upper error bar on  $r$  can be large because the light curve data is compatible with a grazing eclipse by a larger object. This is the case of OGLE-TR-12, 17

and 55. 2) If the primary is not in synchronous rotation, then  $R$  and  $M$  are much more weakly constrained by equations 5 and 6. In that case the influence of the adequacy of the stellar evolution models becomes more important. This is the case of OGLE-TR-34.

## 5. Results

In this section we present our results of Doppler follow-up and light curve analysis. Figure 6, 7, 8, and 9 show the radial velocity data phased with the period from Udalski et al. (2002a, 2002b), or, in the case of OGLE-TR 8, 12, 17, 35, and 59, with the modified period obtained from our analysis. If the radial velocity variations are caused by the transiting objects, then phase  $\phi = 0$  must correspond to the passage of the curve at center-of-mass velocity with decreasing velocity, which provides a further constraint. Results of the fit of the transit shape are summarized in Table 3. Notice that we deliberately do not provide the results for the 4 unsolved cases suspected to be false positives. For the two cases of grazing eclipsing binaries, the stellar parameters were not deduced from the light curve (except the impact parameter  $b$ ) but from the spectroscopic orbits and the rotational velocities.

We distinguish 5 classes of objects, the low mass star transiting companions, the grazing eclipsing binaries, the triple systems, the planetary candidates, and the unsolved cases. For the majority of objects, we used the photometric ephemeris given by Udalski et al. (2002a, 2002b) and updated ephemeris available from the OGLE website<sup>2</sup>. We fixed the transit epoch  $T_0$  and fit the phased radial velocity with a circular orbit. In this way, we determined an updated or corrected period  $P$ , the velocity offset  $V_0$ , and the velocity semi-amplitude  $K$ . Each classes of objects are described in the following subsection and the derived masses and radii are presented and discussed in section 6.

### 5.1. low mass star transiting companions

The orbital parameters we derived for the 8 low mass transiting stellar companions OGLE-TR-5, 6, 7, 12, 17, 18, 34 and 55 are reported in Table 4 and Fig 6.

OGLE-TR-5: This candidate is rotating very rapidly ( $v \sin i \sim 88 \text{ km s}^{-1}$ ), in synchronization with its very short orbital period (0.8 days). Systematic ellipsoidal variations in the light curve reveal the deformation of the primary and therefore the massive nature of the secondary. The mass obtained from the transit duration and radial velocity semi-amplitude is compatible with the spectral type and radius for a G+M binary, and all parameters can be determined precisely.

OGLE-TR-6: The synchronized rotation of this target allows a precise determination of its radius. The transit shape shows that the impact parameter is small, and therefore all parameters can be computed precisely with our "standard" procedure.

OGLE-TR-7: The synchronized rotation of this target allows a precise determination of its radius. The transit shape shows

that the impact parameter is small, and therefore all parameters can be computed precisely with our "standard" procedure. The computed values of  $R$  and  $M$  are compatible with the spectral type for a main-sequence F dwarf.

OGLE-TR-12: The radial velocity data show that this candidate is a binary system with a period 1.5 times greater than the period reported by Udalski et al. (2002a). This value is fully compatible with the light curve. The rotation is synchronized with the orbital period. The light curve indicate that the impact parameter  $b$  is probably high, causing increased uncertainties on  $r$  due to the degeneracy between impact parameters and the  $\bar{r}$  factor. The large uncertainties are of course also due to the fact that there are only two nights in the transit. OGLE-TR-12 was observed with UVES (white points) and FLAMES (dark points). The velocity offset determined between the two set of data indicates a difference of  $0.200 \text{ km s}^{-1}$  between the two instruments.

OGLE-TR-17: The radial velocity data show that this target is a binary system with  $P=13.8736$  days, 6 times the value in Udalski et al. (2002a). This revision is compatible with the light curve data. The estimated rotation velocity of OGLE-TR-17 seems to indicate that this star is not synchronized which is not so surprising considering its quite large period. The shape of the transit allows high values of  $b$ , therefore causing degeneracy between the parameters. Moreover, the poor phase coverage of the transit increases the uncertainties. The large O-C residuals clearly indicate a departure from the circular orbit and a complete Keplerian fit indicate a small but significant eccentricity of  $0.074 \pm 0.008$ . Note that OGLE-TR-17, with the longest period, is the only candidate which present a significant eccentricity.

OGLE-TR-18: The rotation velocity is compatible with synchronous rotation. The fit of the transit parameters yield a high value of  $b$ , which increases the uncertainty on  $r$ .

OGLE-TR-34: The radius given by the rotation velocity assuming synchronization ( $R = 1.02 \pm 0.04 R_{\odot}$ ) is in conflict with the spectral type ( $R > 1.25 R_{\odot}$ ) and the light curve fit ( $R \sim 1.9 R_{\odot}$ ). Releasing the synchronism assumption appears to be the most likely possibility taking into account the quite large period (8.6 days). In that case all the parameters are coherent and well determined. The radius and temperature obtained would put OGLE-TR-34 at the evolved edge of the F main sequence. It is possible that the radius increase at the end of the main-sequence stage has been too rapid to allow synchronization to keep pace, so that the conservation of angular momentum has slowed the rotation down to the observed value. Alternatively, the star could be too young for synchronization to have taken place yet given the 8.6 days period.

OGLE-TR-55: The rotation velocity shows synchronization with the orbital period. The light curve, however, does not constrain the parameters with enough accuracy to confine the value of the impact parameter  $b$ . Because of the large line broadening caused by the high rotation velocity, our spectral type analysis yields only a broad estimate of the spectral type: F5-G8. The uncertainties on the resulting values  $r$  and  $m$  are correspondingly large.

<sup>2</sup> [http://bulge.princeton.edu/~ogle/ogle3/transits/transit\\_news.html](http://bulge.princeton.edu/~ogle/ogle3/transits/transit_news.html)

**Table 4.** Orbital parameters of the low mass star transiting companions, the grazing eclipsing binaries and the triple systems. For the triple systems, the component *a* correspond here to the contaminating third body with fixed parameters and component *b* to the primary of an eclipsing binary with fitted parameters. <sup>1</sup> Residuals of OGLE-TR-17 without and with eccentricity ( $e=0.074$ ). <sup>2</sup> This value corresponds to the anti-transit epoch, the revised value is 74.65125.

Name	$P_{OGLE}$ [days]	$T_{OGLE}$ −2452000	$P$ [days]	$K$ [ $\text{km s}^{-1}$ ]	$V_0$ [ $\text{km s}^{-1}$ ]	$O-C$ [ $\text{km s}^{-1}$ ]
5	0.8082	60.47118	0.808271	$49.90 \pm 2.0$	$16.1 \pm 1.4$	3.5
6	4.5487	61.05651	4.54881	$32.09 \pm 0.15$	$15.33 \pm 0.10$	0.21
7	2.7179	61.42566	2.71824	$31.39 \pm 0.22$	$-10.94 \pm 0.16$	0.37
12	5.7721	61.53515	8.65725	$34.862 \pm 0.025$	$24.255 \pm 0.019$	0.083
17	2.3171	62.35748	13.8737	$31.99 \pm 0.19$	$-34.36 \pm 0.12$	0.894/0.072 <sup>1</sup>
18	2.2280	61.07501	2.228025	$46.87 \pm 1.48$	$-46.75 \pm 1.03$	2.08
34	8.5810	62.74970	8.57633	$32.68 \pm 0.27$	$65.50 \pm 0.20$	0.426
55	3.18456	77.05049	3.184543	$28.63 \pm 0.32$	$5.06 \pm 0.19$	0.439
8a	2.7152	61.01604	5.432842	$79.13 \pm 0.14$	$-3.71 \pm 0.07$	0.260
8b	2.7152	61.01604	5.432842	$82.10 \pm 0.15$	$-3.71 \pm 0.07$	0.299
35a	1.2599	60.98942	2.519569	$104.57 \pm 0.38$	$-61.53 \pm 0.22$	0.521
35b	1.2599	60.98942	2.519569	$104.21 \pm 0.37$	$-61.53 \pm 0.22$	0.611
33a	1.9533	60.54289	-	0.0	−28.5	-
33b	1.9533	60.54289	1.95327	$59.8 \pm 2.1$	$-29.8 \pm 1.3$	3.2
59a	1.49709	73.15416	-	0.0	9.05	0.495
59b	1.49709	73.15416 <sup>2</sup>	2.9943224	$58.68 \pm 0.31$	$6.01 \pm 0.22$	0.524

## 5.2. grazing eclipsing binaries

The orbital parameters we derived for the 2 grazing eclipsing binaries OGLE-TR-8 and 35 are reported in Table 4 and Fig 7.

OGLE-TR-8: The cross-correlation function of the spectra shows two components of approximately equal intensity, varying along a SB2 orbit of two times the period given by Udalski et al. (2002a), which reveals that both the eclipse and anti-eclipse of comparable magnitude were visible in the light curve. The rotation velocities show synchronous rotation on both components. The  $M \sin i$  of both components are computed from the radial velocity curve, the  $R \sin i$  from the rotation velocity and period, and the  $i$  angle from the light curve. The eclipse has to be grazing because the components are of similar size and the depth of the eclipse is only a few percent. This constraint alone fixes  $\sin i$  within a very small interval. All parameters are therefore determined with very high accuracy, showing that OGLE-TR-8 is a G-G grazing binary.

OGLE-TR-35: The spectroscopic data show that this target is a double-line binary with a period double that given by Udalski et al. (2002a). Therefore, both the eclipse and anti-eclipse are visible in the light curve. As for OGLE-TR-8, the combination of the radial velocity orbits, the two rotation velocity and the transit depth fix all the parameters very precisely. OGLE-TR-35 is a F-F grazing binary.

## 5.3. Low mass star transiting companions in triple systems

The orbital parameters we derived for the 2 triple systems OGLE-TR-33 and 59 are reported in Table 4 and Fig 8. To determine the characteristic of the second component, we subtracted in the CCF a fixed Gaussian or a fixed rotational profile.

OGLE-TR-33: As discussed by Konacki et al. (2003b), this candidate presents a clear blend effect visible in the line bisector as well as in the asymmetry of the bottom of the CCF. This object consists in a triple system, i.e. an eclipsing binary and a contaminating third body. In order to characterize the second spectral component, we subtracted a constant rotational profile to the CCF. The second component seems to have a rotation velocity synchronized with the orbital period and is in phase with the Udalski et al. (2002a) period. The amplitude of the radial velocity variations indicates a low mass star transiting companion. A detailed analysis of this system, in full agreement with our result, have been made recently by Torres et al. (2004b).

OGLE-TR-59: This target has a double-line spectra. However, only one set of lines shows large radial velocity variations and presents a period double that given by Udalski et al. (2002b). The transit epoch has to be shifted by half a revised period. Therefore, this object consists in a triple system, with an eclipsing binary and a contaminating third body, either the component of a physical triple system, or an unrelated background/foreground star. The fixed component represents  $\sim 70$  percent of the CCF surface, and the eclipsed object 30 percent. If the eclipsed object is in synchronous rotation, its rotation velocity implies  $R = 0.624 \pm 0.033 R_{\odot}$ . The transit curve is clearly V-shaped, indicating a grazing eclipse, so that the radius ratio of the eclipsed component to the eclipsing body is not strongly constrained. If that component obeys the  $M \sim R$  relation of M dwarfs, then the amplitude of the radial velocity variations imply  $m \sim 0.30 M_{\odot}$ . Therefore the system would consist of a M-M binary with a F/G contaminant in the background. With the present data other scenarios are difficult to exclude entirely.

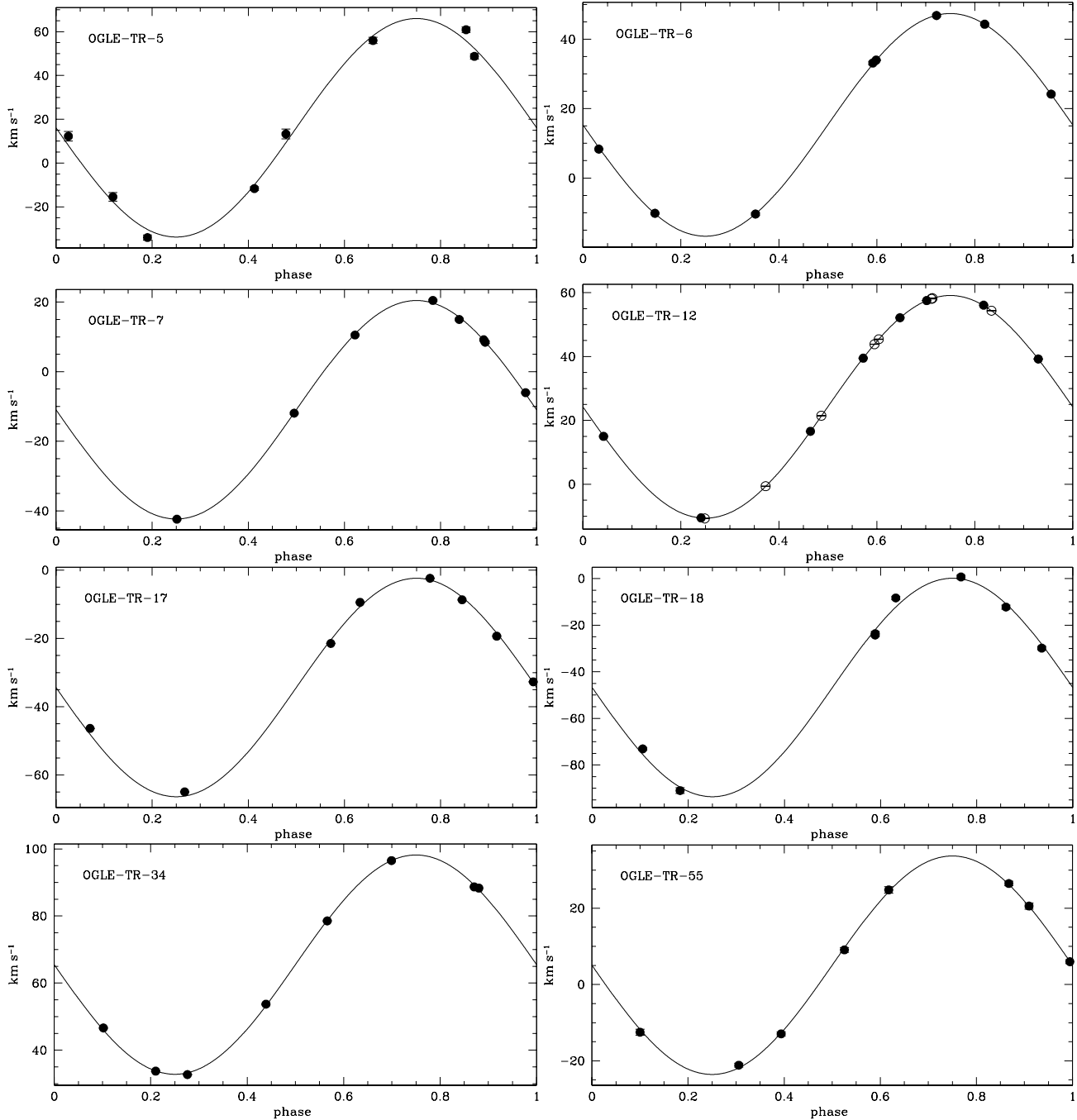


**Fig. 6.** Phase-folded radial velocities of the low mass star transiting companions. For OGLE-TR-12, black and white points correspond respectively to FLAMES and UVES measurements.

#### 5.4. Planetary transits, unsolved cases and false positives

Six of our targets show radial velocity variations lower than  $1 \text{ km s}^{-1}$ , or comparable with the error bars, indicating the possibility that the transit signal is caused by a planet-mass companion. Of these however, only one exhibits the signature of a clear orbital motion - the known planetary system OGLE-TR-56 (Konacki et al. 2003a, Torres et al. 2004a). For OGLE-TR-10, a planetary explanation is proposed. For 3 other targets, our data do not allow us to conclude but we strongly suspect a false

positive transit detection as already examined in section 4.1. For OGLE-TR-58 we present strong evidence of a false positive transit detection.

The orbital parameters we derived for the 6 candidates harboring low radial velocity variations OGLE-TR-10, 19, 48, 49, 56 and 58 are reported in Table 5 and Fig 9. For these candidates we fixed the period given and updated by the OGLE team.

**OGLE-TR-10:** This candidate was observed with UVES (white points) and FLAMES (black points). The UVES radial velocity was corrected from the offset velocity of

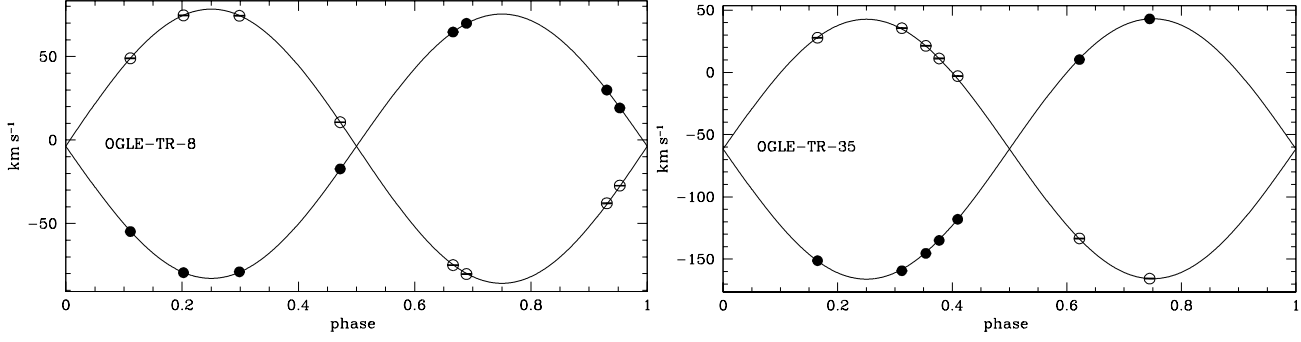


**Fig. 7.** Phase-folded radial velocities of grazing eclipsing binaries. Black and white points correspond respectively to component *a* and *b*.

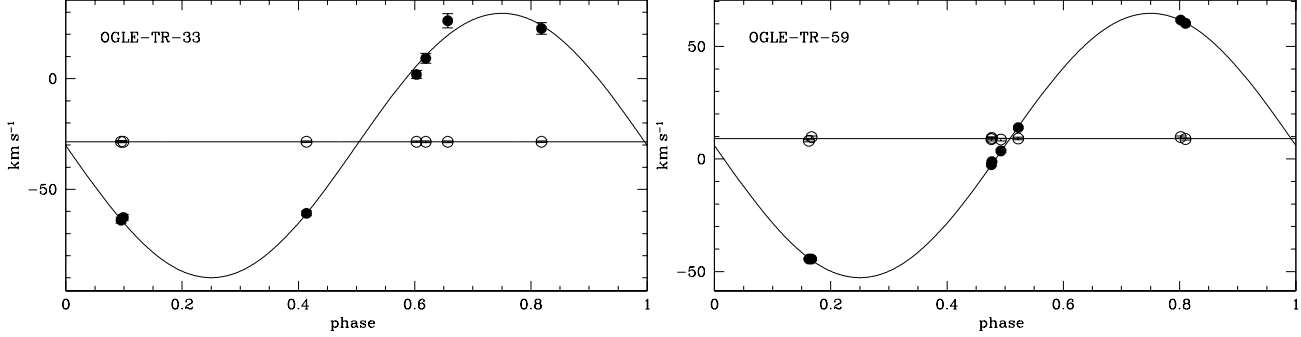


**Fig. 8.** Phase-folded radial velocities of triple system. Black and white points correspond respectively to component *b* and *a*.

**Table 5.** Orbital parameters of planetary candidates, unsolved cases and false positives.

Name	$P_{OGLE}$ [days]	$T_{OGLE}$ -2452000	$K$ [ $\text{km s}^{-1}$ ]	$V0$ [ $\text{km s}^{-1}$ ]	O-C [ $\text{km s}^{-1}$ ]
10	3.1014	70.2190	$0.081 \pm 0.025$	$-6.246 \pm 0.017$	0.068
19	5.2821	61.89798	$0.146 \pm 0.048$	$-33.280 \pm 0.033$	0.074
48	7.2255	74.19693	-	$2.30 \pm 1.45$	2.9
49	2.69042	75.53363	-	$-106.90 \pm 0.10$	0.286
56	1.2119189	75.1046	$0.212 \pm 0.022$	$-48.324 \pm 0.018$	0.051
58	4.34244	76.81982	-	$51.08 \pm 0.025$	0.072

$0.200 \text{ km s}^{-1}$  as determined on OGLE-TR-12. Note that the two higher values of UVES were made under “unfavorable” seeing conditions (seeing lower than 0.9 arcsec) and are not taken into account afterward. The fit indicates an orbital signal with  $K = 81 \pm 25 \text{ m s}^{-1}$  which corresponds to a  $0.66 \pm 0.21$  Jupiter mass companion. The reduced  $\chi^2$  is 2.3 for a constant velocity curve and 1.4 for a circular orbit. The analysis of the transit shape and the spectroscopic parameters lead to  $r = 1.54 \pm 0.12 R_{\text{Jup}}$ . Such a planet, if confirmed, would have a density quite lower than HD209458. It is also quite interesting to note that OGLE-TR-10 presents an excess of metallicity, as it is well known that the planet-hosts discovered using radial-velocity techniques are, in average, significantly more metal-rich than average field dwarfs (e.g. Santos et al. 2001). In order to examine the possibility that the radial velocity variation is due to a blend scenario, we computed the CCF bisectors as described by Santos et al. (2002). We did not find any significant bisector effect in the CCF. We also checked the influence of the cross-correlation mask used in the CCF computation and did not find any ef-

fect. However further observations are needed to confirm our hypothesis and a blend scenario could not completely be excluded considering the low SNR of our data. Both our observations and the possibility of a blend scenario are in agreement with Konacki et al. (2003b).

**OGLE-TR-19:** The phase-folded Doppler measurements indicates a significant variation. The reduced  $\chi^2$  is 2.3 for a constant velocity curve and 0.7 for a circular orbit. The fit gives an orbit with  $K = 146 \pm 48 \text{ m s}^{-1}$  which correspond to a  $1.2 \pm 0.4$  Jupiter mass companion. The rotation velocity is comparable with the instrumental broadening, so that synchronous rotation is excluded. The analysis of the transit shape gives  $\bar{r} = 0.343$  and  $b$  in the range  $[0.79-1.09]$ . The spectroscopic parameters indicate  $R = 1.46 \pm 0.16 R_{\odot}$  and  $M = 0.92 \pm 0.05 M_{\odot}$ , implying  $r = 4.9 \pm 1.1 R_{\text{Jup}}$ . Such a radius is much larger than any planet model would predict, and reinforces the odds against the planetary explanation. A single star blended with a background eclipsing binary would probably explain the data more convincingly. Our bisectors analysis, limited by the high uncertainties, cannot

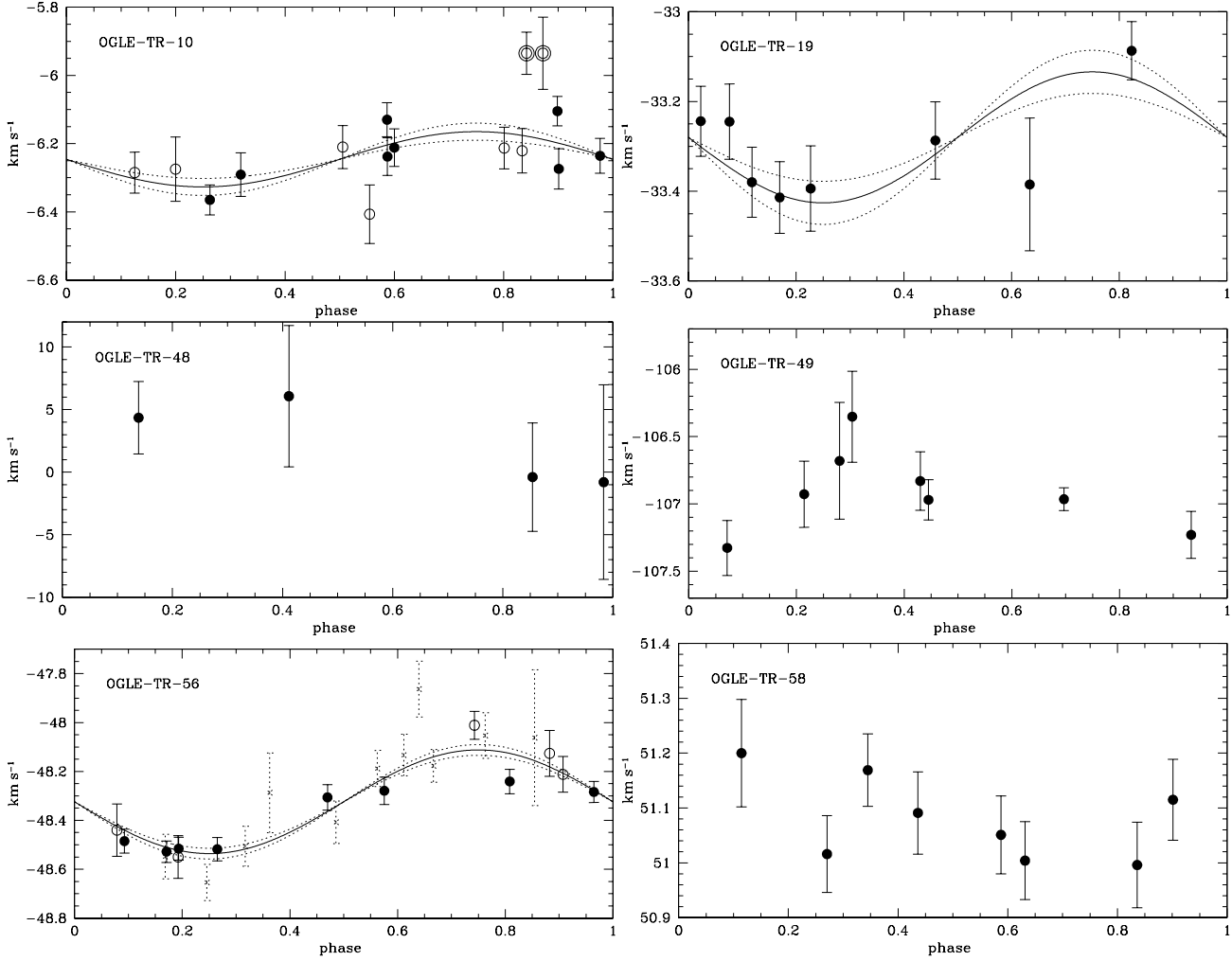


**Fig. 9.** Phase-folded Doppler measurements of planetary candidates and unsolved cases. For OGLE-TR-10, black and white points correspond respectively to FLAMES and UVES measurements. Encircled points correspond to measurements made with a seeing lower than 0.9 arcsec. For OGLE-TR-56, black, white and dotted cross points correspond respectively to FLAMES, HARPS and Torres et al. (2004a) measurements. For OGLE-TR-10, 19 and 56, the dotted lines correspond to fit curves for lower and upper 1-sigma intervals in semi-amplitude  $K$ .

exclude such a scenario. Alternatively, we note that only two transits were observed for this candidates (see Fig. 3 and Fig. 10), which puts OGLE-TR-19 among the less secure transit candidates. The “false positive” transit detection could not be excluded and only additional photometric and Doppler measurements will allow a definitive conclusion.

**OGLE-TR-48:** The spectroscopic data reveal that this target is a very rapid rotator, with  $V_{rot} > 100 \text{ km s}^{-1}$ . Consequently, only very approximate radial velocities could be computed from the spectra on only half of the spectra. These measurements do not show significant variations within the  $\sim 10 \text{ km s}^{-1}$  accuracy. The rotation is not synchronous with the transit period for any reasonable value of the primary radius. We suspect that this very high rotation indicates a A or early F star and considering the radius ratio of about 0.14, it seems unlikely that the transit could be due to a planetary companion. The upper limit on the radial velocity variations exclude a companion with mass larger than

$\sim 0.15 M_{\odot}$ . However, because only two partial transits were observed in the light curve (see Fig. 3 and Fig. 10), it is not possible to be confident at this stage in the validity of the transit period. The most likely explanation is that one or both detected transits are spurious.

**OGLE-TR-49:** No velocity variation in phase with the transit period and no synchronous rotation are observed for this candidate. The reduced  $\chi^2$  is 1.6 for a constant velocity curve. Only two transits were observed in the light curve (see Fig. 3), which puts OGLE-TR-49 among the less secure transit candidates. The interval between the two transits is  $\Delta T = 21.52$  days (8 times the period proposed by Udalski et al. 2002b). If we adopt this largest period, radial velocity gives  $K < 200 \text{ m s}^{-1}$ . The transit is poorly defined and the uncertainties on the transit parameters are large. The spectroscopic parameters do not allow strong constraint on the mass and radius of the primary. Our data can unfortunately not exclude a planetary companion nor an explanation in terms of a background eclipsing binary.

However, inspection of the light curve (see Fig. 10) favors an explanation in terms “false positive” transit detection.

**OGLE-TR-56:** This candidate was observed with FLAMES (black points) and the HARPS spectrograph (white points). The phase-folded Doppler measurements indicate a clear variation. The reduced  $\chi^2$  is 9.1 for a constant velocity curve and 1.1 for a circular orbit. The fit gives an orbit with  $K = 212 \pm 22 \text{ m s}^{-1}$  which correspond to a  $1.18 \pm 0.13 \text{ Jupiter mass companion}$ . The analysis of the transit shape and the spectroscopic parameters lead to  $r = 1.25 \pm 0.09 R_{\text{Jup}}$ . We do not find any bisector effect in the CCF nor influence of the cross-correlation mask used. Our characterization of OGLE-TR-56b is in agreement (within the error bars) with the revised value given by Torres et al. (2004a) and clearly confirm the planetary nature of this object.

**OGLE-TR-58:** This target shows no radial velocity variation and no synchronous rotation. The reduced  $\chi^2$  is 1.0 for a constant velocity curve. The suspicion of a spurious transit signal in the light curve is even stronger as for the previous objects, because the signal detection confidence is the lowest of the whole Udalski et al. (2002a, 2002b) sample, and the light curve shows obvious signs of variability to the level of the hundredth of magnitude. As already noted by Konacki et al. (2003b) and Sirko & Paczynski (2003), the mean level has increased by 0.02 mag between one season and the next. Only two possible transits were detected, one in a night showing a clear *increase* of flux before the transit – so that the average flux over the night is not lower than the normal level for OGLE-TR-58 – and the other consisting of a whole night at lower flux, not a very constraining transit signal (see Fig. 10). We therefore conclude that OGLE-TR-58 is a “false positive” of the transit detection algorithm.

## 6. Discussion and conclusion

Table 6 summarizes all the available information derived for our objects following our procedure described in section 4.4. The variety of cases encountered in our sample of eighteen objects is striking and covers a large part of the bestiary of possible contaminations in the search for planetary transits. Target OGLE-TR-5, 6, 7, 12, 17, 18, 34, and 55 have clear resolved orbits of eclipsing binaries with a large F/G primary and a small M transiting companion. OGLE-TR-8 and 35 have clear resolved orbits of equal-mass, grazing eclipsing binaries. OGLE-TR-33 and 59 have resolved orbits of eclipsing binaries in a hierarchical triple system. OGLE-TR-56 shows small radial velocity variations in agreement with Torres et al. (2004a) which confirm the planetary nature of the transiting companion. OGLE-TR-10 shows small radial velocity variations which could be due to planetary companion. OGLE-TR-19, 48 and 49 are unfortunately not yet solved but we strongly suspect false positive transit detections. OGLE-TR-58 shows no radial velocity variations and its light curve presents clear indication that the detected photometric signal is not a bona fide transit. Note that in some cases (OGLE-TR-12, 17 and 59), the initial period identified from the light curve was not correct and that

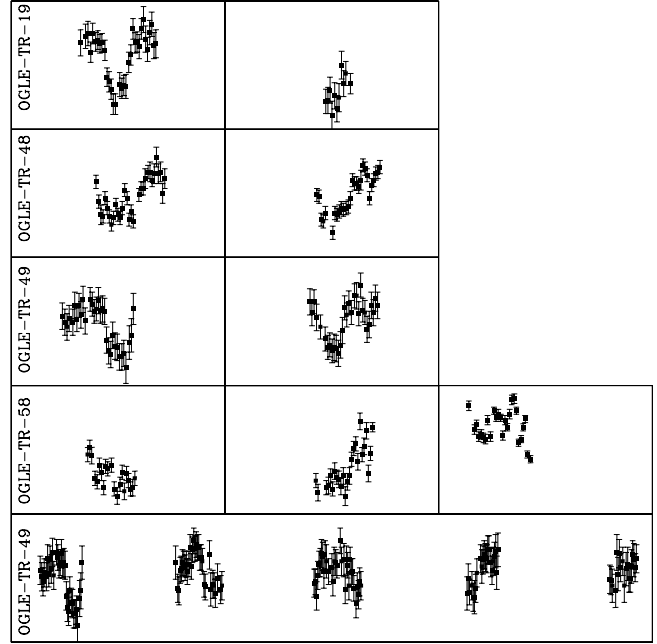


**Fig. 10.** Light curve data during the night of detected transits for OGLE-TR-19, 48, 49, and 58 (from top to bottom) and light curve of OGLE-TR-49 for some days after the first detected transit (bottom). The correlation of the residuals is clearly visible in the other nights as well.

in many cases our secondary radius are very different from the initial value of Udalski et al. (2002a, 2002b).

Our study has yielded precise radii and masses for a certain number of low mass star companions. The mass-radius relation for these objects is given in the Fig. 11. We note that no brown-dwarves were detected in our sample in agreement with the so-called brown dwarf desert for the short period companions. No stellar companions were detected in the mass domain  $0.6\text{--}1.0 M_{\odot}$  due to the fact that we selected in priority the smallest candidates of the OGLE survey. OGLE-TR12, 17 and 55 (white points) needs additional photometric measurements in order to properly constrain the impact parameter  $b$  of the transits. For the other 5 low mass star transiting companions, the precision on the radius and mass determination are respectively on the range 4.5–10% and 7–13%. This precision is not at the level needed to provide a crucial test of stellar physics (e.g., Andersen 1991). However the empirical Mass-Radius relation remains poorly constrained due to the lack of observations of M-type eclipsing binaries. These 5 new candidates significantly increase the number of known M-type eclipsing binaries and give new observational constraints on models. For comparison we added on Fig. 11 the three known M-type eclipsing binaries (Metcalf et al. 1996, Torres & Ribas 2002, Ribas 2003). Although characterized with a significantly lower accuracy, our 5 low mass stars seems to follow the same departure from models.

The OGLE fields are very crowded, and some of the targets are expected to be contaminated by background stars (or foreground fainter stars). Extrapolating the density of bright stars to fainter magnitudes indicates that there may be on average

**Table 6.** Summary table with the physical parameters  $r$ ,  $R$ ,  $m$  and  $M$ , the orbital angle  $i$  and the identification of the system.

Name	$r$ [ $R_{\odot}$ ]	$R$ [ $R_{\odot}$ ]	$m$ [ $M_{\odot}$ ]	$M$ [ $M_{\odot}$ ]	$i$	comments
5	$0.263 \pm 0.012$	$1.39 \pm 0.026$	$0.271 \pm 0.035$	$1.12 \pm 0.21$	81-90	G-M binary
6	$0.393 \pm 0.018$	$1.99 \pm 0.068$	$0.359 \pm 0.025$	$1.37 \pm 0.14$	88-90	F-M binary
7	$0.282 \pm 0.013$	$1.64 \pm 0.052$	$0.281 \pm 0.029$	$1.32 \pm 0.21$	86-90	F-M binary
8	$1.217 \pm 0.035$	$1.27 \pm 0.035$	$1.160 \pm 0.010$	$1.20 \pm 0.010$	86	G-G SB2
10	$0.156 \pm 0.012$	$1.21 \pm 0.066$	$0.00063 \pm 0.00020$	$1.22 \pm 0.045$	87-90	possible planet
12	$0.440 [0.380-1.089]$	$1.47 \pm 0.065$	$0.492 \pm 0.026$	$1.28 \pm 0.10$	85	F-M binary
17	$0.371 [0.325-0.956]$	$1.52 \pm 0.110$	$0.482 \pm 0.040$	$1.06 \pm 0.13$	86-88	F-M binary
18	$0.390 \pm 0.040$	$1.95 \pm 0.042$	$0.387 \pm 0.049$	$1.18 \pm 0.22$	79-86	F-M binary
19	-	-	-	-	-	unsolved case
33	-	-	-	-	-	blend
34	$0.435 \pm 0.033$	$2.31 \pm 0.174$	$0.509 \pm 0.038$	$1.56 \pm 0.17$	86-90	F-M binary
35	$1.74 \pm 0.039$	$1.71 \pm 0.054$	$1.200 \pm 0.009$	$1.19 \pm 0.009$	80-81	F-F SB2
48	-	-	-	-	-	unsolved case
49	-	-	-	-	-	unsolved case
55	$0.209 [0.204-0.989]$	$1.92 \pm 0.036$	$0.276 \pm 0.038$	$1.36 \pm 0.28$	81-90	F-M binary
56	$0.128 \pm 0.009$	$1.12 \pm 0.069$	$0.00113 \pm 0.00013$	$1.10 \pm 0.078$	81-83	confirmed planet
58	-	-	-	-	-	false positive
59	-	-	-	-	-	blend

1.4 contaminants stars per object down to  $\Delta mag = 6$ . Bright contaminant would be detected by the spectroscopy, but faint contaminants can go unnoticed and contribute a few percent to the light curve. This makes the photometric transit depth shallower, leading to an underestimation of  $\bar{r}$ . Note that this effect is seeing dependent.

The effect of different assumptions on limb darkening on the derivation of the parameters from the light curve were verified using OGLE-TR-6 (central transit) and OGLE-TR-55 (grazing eclipse). Changing  $u1+u2$  by 0.2 leads to a difference of the order of 2% on  $\bar{r}$  and on  $V_T/R$ , while removing the limb darkening entirely changes  $\bar{r}$  and  $V_T/R$  by  $\sim 8\%$ . We also test the effect of changing the limb darkening law in the derivation of the rotation velocity from the CCF. Using coefficients  $u1+u2=0.3$  instead of  $u1+u2=0.6$  modifies  $V_{rot} \sin i$  by about 3%.

This program illustrates the capability of ground-based spectrographs like FLAMES, UVES and HARPS to follow the faint transiting candidates found by photometric surveys. It demonstrates the usefulness of such a Doppler follow-up in order to discriminate among a large sample of possible contaminations in the search for planetary systems. We used in average only 2.5 hours of observing time per object, thanks essentially to the very high efficiency of the FLAMES multi-fibers facility. Our analysis shows that a large part of the transiting candidates could be rejected even a priori through a fine-tuned light curve analysis (confidence factor, sinusoidal variations and transit shape). It is also clear that more accurate measurements in both photometry and radial velocity will be very useful in order to provide stronger constraints on the mass and radius of transiting companions, especially for the suspected planetary system OGLE-TR-10, for the unsolved cases OGLE-TR-19 and 49 and for the unconstrained radius of the companions of OGLE-TR-12, 17 and 55.

**Acknowledgements.** We are grateful to J. Smoker for support on FLAMES at Paranal. F.P. gratefully acknowledges the support of CNRS through the fellowship program of CNRS. F.B. acknowledges P. Le Strat for continuous support and advices. Support from Fundação para a Ciência e Tecnologia (Portugal) to N.C.S. in the form of a scholarship is gratefully acknowledged.

## References

- Andersen, J., 1991, A&A Rev., 3, 91  
Baraffe, I., Chabrier, G., Allard, F., & Hauschildt, P.H., 1998, A&A, 337, 403  
Barban, C., Goupil, M.J., Van't Veer-Menneret, C., et al., 2003, A&A, 405, 1095  
Bouchy, F., Pont, F., Santos, N.C., et al., 2004, A&A, 421, L13  
Brown, T.M., Charbonneau, D., Gilliland, R., et al., 2001, ApJ, 552, 699  
Charbonneau, D., Brown, T.M., Latham, D., & Mayor, M., 2000, ApJ, 529, L45  
Dreizler, S., et al., 2002, A&A, 391, L17  
Dreizler, S., Hauschildt, P.H., Kley, W., et al. 2003, A&A, 402, 791  
Eggenberger, A., Udry S., Mayor, M., 2004, A&A, 417, 353  
Girardi, M., Manzato, P., Mezzetti, M., et al., 2002, ApJ, 569, 720  
Goldreich, P. & Tremaine, S., 1980, ApJ, 241, 425  
Guillot, T., 1999, Science, 286, 72  
Henry, G., Marcy, G., Butler, R. & Vogt, S., 2000, ApJ, 529, L41  
Horne, K., 2003, ASP Conf. Series, 294, 361  
Hut, P., 1981, A&A, 99, 126  
Konacki, M., Torres, G., Jha, S., et al., 2003a, Nature, 421, 507;  
Konacki, M., Torres, G., Sasselov, D., et al., 2003b, ApJ, 597, 1076  
Kurucz, R., 1993, ATLAS9 Stellar Atmospheres Programs and 2 km s<sup>-1</sup> Grid, CD-ROM No. 13. (Cambridge: Smithsonian Astrophys. Obs.)  
Levato, H., 1976, ApJ, 203, 680  
Lin, D.N.C., Bodenheimer, P., Richardson, D.C., 1996, Nature, 380, 606  
Mandel, K. & Agol, E., 2002, ApJ, 580, 171  
Mayor, M., Pepe, F., Queloz, D., et al., 2003, The Messenger, 114, 20  
Mazeh, T., Naef, D., Torres, G., et al., 2000, ApJ, 532, L55



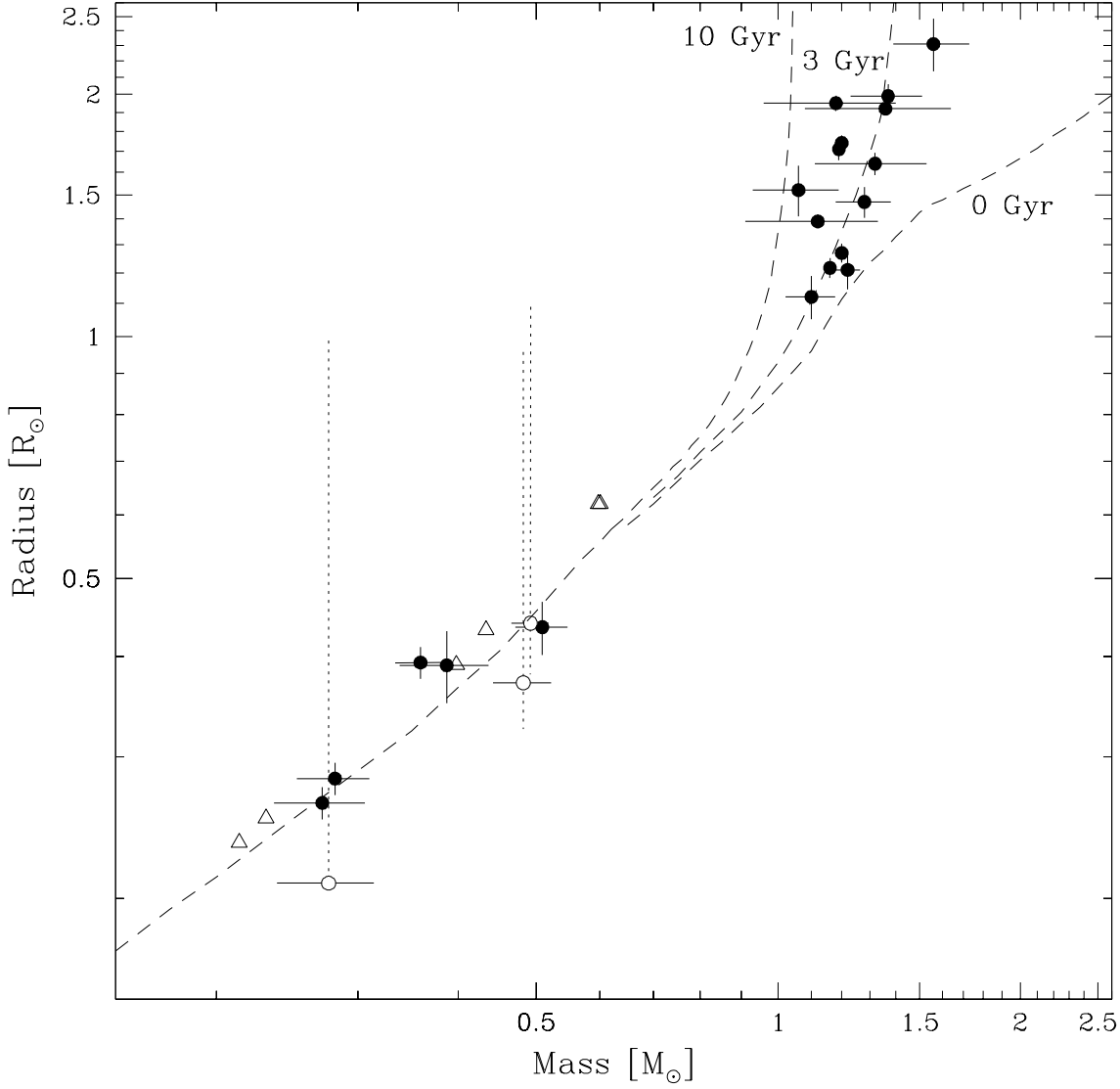


**Fig. 11.** The mass-radius relation for all stellar objects in our sample, primary and secondary. Open circles correspond to candidates OGLE-TR-12, 17 and 55 with a wide range of possible radius. Triangles correspond to the three known M-type eclipsing binaries. The dashed curve up to  $0.6 M_{\odot}$  corresponds to the 1 Gyr theoretical isochrones of Baraffe et al. 1998. Above  $0.6 M_{\odot}$  the 3 dashed curves show the Padova model mass-radius relations for solar metallicity for three age values.

Melo, C.H.F., Covino, E., Alcalá, J.M., Torres, G., 2001, *A&A*, 378, 898

Metcalfe, T.S., Mathieu, R.D., Latham, D.W., & Torres, G., 1996, *ApJ*, 456, 356

Moutou, C., Pont, F., Bouchy, F., Mayor, M., 2004, *A&A*, 424, L31

Pont, F., Bouchy, F., Santos, N.C., et al., 2004, *A&A*, in press

Ribas, I., 2003, *A&A*, 398, 239

Santos, N.C., Israelian, G., Mayor, M., 2001, *A&A*, 373, 1019

Santos, N.C., Mayor, M., Naef, D., et al., 2002, *A&A*, 392, 215

Santos, N.C., Mayor, M., Udry, S., et al., 2003, *A&A*, 398, 363

Santos, N.C., Israelian, G., Mayor, M., 2004, *A&A*, 415, 1153

Snedden, C., 1973, Ph.D. Thesis, University of Texas

Sirko, E. & Paczynski, B., 2003, *ApJ*, 592, 1217

Torres, G., & Ribas, I., 2002, *ApJ*, 567, 1140

Torres, G., Konacki, M., Sasselov, D., et al., 2004a, *ApJ*, 609, 1071

Torres, G., Konacki, M., Sasselov, D., et al., 2004b, *ApJ*, in press

Udalski, A., Paczynski, B., Zebrun, K., et al., 2002a, *Acta Astronomica*, 52, 1

Udalski, A., Zebrun, K., et al., 2002b, *Acta Astronomica*, 52, 115

Udalski, A., Zebrun, K., et al., 2002c, *Acta Astronomica*, 52, 317

Udalski, A., Pietrzynski, G., et al., 2003, *Acta Astronomica*, 53, 133

Udry S., Mayor, M., Santos, N.C., 2003, *A&A*, 407, 369